Ocean Engineering 184 (2019) 59–73

Contents lists available at ScienceDirect

Ocean Engineering

journal homepage: www.elsevier.com/locate/oceaneng

Spatial coherence of ocean waves in multiline anchor systems for floating offshore wind turbines

Casey M. Fontana [a,*], Spencer T. Hallowell [a], Sanjay R. Arwade [a], Don J. DeGroot [a], Melissa E. Landon [b], Charles P. Aubeny [c], Andrew T. Myers [d]

[a] University of Massachusetts Amherst, Marston Hall, 130 Natural Resources Road, Amherst, MA, 01003, USA
[b] University of Maine, 319B Boardman Hall, Long Road, Orono, ME, 04469, USA
[c] Texas A&M University, 199 Spence Street, College Station, TX, 77840, USA
[d] Northeastern University, 439 Snell Engineering Center, 360 Huntington Avenue, Boston, MA, 02115, USA

ARTICLE INFO

Keywords:
Floating turbines
Wind energy
Spatial waves
Wave coherence
Multiline anchors
Turbine spacing

ABSTRACT

A shared multiline anchor system may reduce material and installation costs for floating offshore wind farms, but the concept also expands the physical space over which the analysis of the system must be considered. The multiline anchor force is a combination of forces that originate from different floating offshore wind turbine (FOWT) platforms, and this interconnectivity mandates investigation of spatial coherence of waves over the area of the connected turbines. The goal of this work is to determine if anchor force characteristics are sensitive to spatial coherence of the wave field, or if an assumption of independent wave fields at different FOWT locations provides sufficiently accurate anchor load characterizations. Spatially coherent irregular wave fields are generated and applied to FOWT systems in 3-line and 6-line anchor systems, revealing negligible sensitivity of multiline anchor force to wave spatial coherence. These results are continued with a parametric study showing how wave characteristics affect correlation lengths of spatially coherent waves. A review of installed offshore wind turbine spacings is presented as a context for these results. In each section, regular waves are first used to examine the dynamics in a simple context, then irregular waves are used to more realistically simulate ocean conditions.

1. Introduction

As the offshore wind industry trends towards deeper water locations, the need for floating offshore wind technology becomes more important (U.S. Department of Energy, 2016). However, the additional support structure demands present in floating offshore wind turbines (FOWTs) currently prevent them from being cost competitive with fixed-bottom turbines (Mone et al., 2015). One potential way to address this high cost hurdle is a multiline anchor concept, in which FOWTs share anchors to reduce the total number of anchors required, as shown in Fig. 1 (Fontana et al., 2017).

A key difference in this novel anchoring concept is that the forces acting on the multiline anchor come from multiple turbines at several different locations in the wind farm, as compared to the conventional single-line anchor, which only sees forces from one FOWT at one location. This interconnectedness of the system through shared anchor points creates the need to evaluate the loading of the multiline anchors on a multi-turbine, spatio-temporally coherent scale, since demands on the multiline anchor depend on the motions of multiple platforms at different locations in the wind farm.

The goal of this work is to determine if characteristics of the anchor loads are sensitive to spatial coherence of the wave field as it moves through an offshore floating wind farm, or whether an assumption of independence of the wave fields at different FOWT locations provides sufficiently accurate anchor load characterizations. This investigation of spatial wave coherence in multiline anchor systems will inform more accurate numerical modeling, an essential task when obtaining meaningful results for this novel system. Determining the importance of spatial wave coherence in multiline anchor force modeling is also a valuable outcome for all future multiline anchor analysis, as the simulations of spatially coherent waves are significantly more complex than those of independent wave fields, especially as the scale of the wind farm and number of wind turbines increase. For the purposes of this study,

* Corresponding author. Department of Civil Engineering, University of Massachusetts Amherst, Marston Hall 236, 130 Natural Resources Road, Amherst, MA, 01003, USA.
E-mail addresses: cfontana@invenergyllc.com, ca.fontana17@gmail.com (C.M. Fontana).

https://doi.org/10.1016/j.oceaneng.2019.04.048
Received 26 August 2018; Received in revised form 15 April 2019; Accepted 20 April 2019
Available online 21 May 2019

Abbreviations

FOWT	Floating Offshore Wind Turbine
WWC	Wind, Wave, Current
SLC	Survival Load Case
JONSWAP	Joint North Sea Wave Project

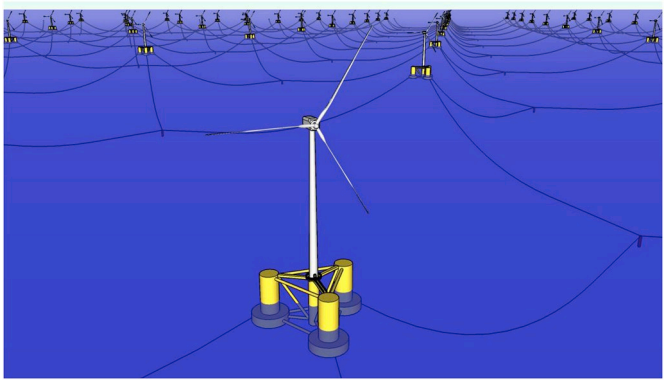

Fig. 1. Multiline anchor system for floating offshore wind farm.

wind fields are assumed to be spatially independent at different FOWT locations. However, wake effects could play a role in governing multiline anchor forces, and this topic is a subject of ongoing study by the authors. Furthermore, directional spreading of the sea state is not considered in any case because unidirectional sea states are assumed to have more impact on the multiline anchor loads.

There are many examinations of spatial wave characteristics in published literature, but far fewer have looked at the wave surface over a large distance, and have mostly been limited to extreme and freak waves. Latifah and Groesen (2012) focused on estimating the position and time of a freak wave event given a time signal and phase information at a certain position. Alvise et al. (2017) analyzed the temporal profile and height of space-time extreme wind waves using real wave data, in efforts to verify estimations of the shape and the crest-to-trough height of near-focusing large 3D wave groups. Other research on spatial characteristics of waves has been focused on the evolution of statistical wavefield parameters. Shemer and Sergeeva (2009) generated unidirectional random waves in 300 m wave tank to analyze changes in the frequency spectrum of the wavefield over the distance of travel. Additionally, Sergeeva et al. (2013) generated numerical simulations of unidirectional spatio-temporal wave evolutions, with a focus on rogue wave occurrence and propagation. As a distinction, one of the novel outcomes of this research is the examination of the correlation coefficient of wave elevation time histories at two different points in space. Furthermore, this research examines wave correlation and coherence over larger distances (>1000 m) than most previous studies.

The results of this study on spatial wave coherence are not limited to use in FOWTs with multiline anchor systems. Design of wave energy converters (WECs) may also benefit from better understanding of spatial wave coherence, as it could potentially be used to optimize the layout within an array such that each WEC experiences the largest waves, and in effect, produces the most power (Balitsky et al., 2017). In addition, wave energy converters may also be a well-suited candidate for multiline anchor system applications.

The role of spatial wave coherence in determining multiline anchor forces is addressed with numerical simulations of a multiline anchor connected to FOWTs loaded by spatially coherent and independent waves. This paper first examines the effect of spatial wave coherence in a multiline anchor system for semisubmersible FOWTs, then expands upon these results with an examination of just-waves realizations (no FOWT) to determine how wave characteristics affect the wave correlation lengths. In both of these sections, regular waves are first used to examine the dynamics in a simple context, then irregular waves are used to more accurately simulate real world conditions. Results are presented in the context of real spacings of installed offshore wind farms.

2. Multiline anchor force

This section examines a multiline anchor connected to FOWTs subjected to both regular and irregular wave loading. In this context, use of the terms in-phase versus out-of-phase to describe waves at the platforms is specific to regular waves, while use of the terms coherent versus independent are specific to irregular waves. The first goal of this section is to establish the range of the multiline anchor force for the case where the platforms connected to the anchor are loaded by in-phase versus out-of-phase regular waves. The following subsection then uses irregular waves to determine if the multiline anchor force dynamics are a function of wave coherence.

2.1. Software and turbine model

Simulation of FOWT dynamics was accomplished with National Renewable Energy Laboratory's computer-aided engineering tool FAST. FAST v8 is a comprehensive, coupled aero-hydro-servo-elastic simulator capable of predicting motions and loads in the time domain (Jonkman and Jonkman, 2016; Jonkman and Buhl Jr., 2005). The turbine chosen for this analysis is the National Renewable Energy Laboratory's (NREL) 5-MW reference turbine, which was developed to be representative of a typical utility-scale turbine, and is widely used in the wind energy research community (Jonkman et al., 2009). The FOWT support structure chosen for this study is the OC4 DeepCwind semisubmersible platform in 200 m water depth (Coulling et al., 2013a,b; Robertson et al., 2014), which is based largely on the DeepCwind scaled test floater (Robertson et al., 2013) and consists of a ballast supported tri-floater with three large cylindrical columns acting as pontoons which are connected to a central main column that supports the tower and rotor nacelle assembly (Robertson et al., 2014). The DeepCwind OC4 semisubmersible floating system was chosen because it employs the most commonly studied platform type (semisubmersible) and mooring system type (catenary) in current FOWT technology/concepts (Carbon Trust, 2015). Mooring line and anchor force dynamics were simulated via MoorDyn, a lumped-mass mooring model within FAST (Hall, 2017). Seabed friction forces on the mooring line are not currently included in this model, and therefore were applied in a post-processing routine outlined in (Fontana et al., 2018). Capturing seabed friction forces in a postprocessing routine is possible for this model since the anchor is treated as a fixed point on the seabed surface, and the reverse catenary curvature of the mooring line under the soil is not considered (Fontana et al., 2018). The hydrodynamics model includes 2nd-order mean-drift and slow-drift effects on the floating platform using the full difference-frequency quadratic transfer functions (Jonkman et al., 2015).

The spatial layouts of the conventional single-line and novel multiline FOWT systems are shown in Fig. 2. The multiline layout was obtained by taking the layout of the default OC4-DeepCwind semisubmersible system and patterning it such that the anchor points overlapped. The key takeaway of this method is that the mooring system layout of each turbine – the distance of each anchor from the turbine - is unchanged between the single-line (Fig. 2a) and the multiline systems (Fig. 2b and c). Patterning the default system in this way results in a turbine spacing of 1451 m. This spatial layout of the mooring system was generated from the default mooring design, and the floating system could of course be designed for different radial distances from fairlead to anchor. The interconnectivity of the turbines in Fig. 2b and c exhibits the

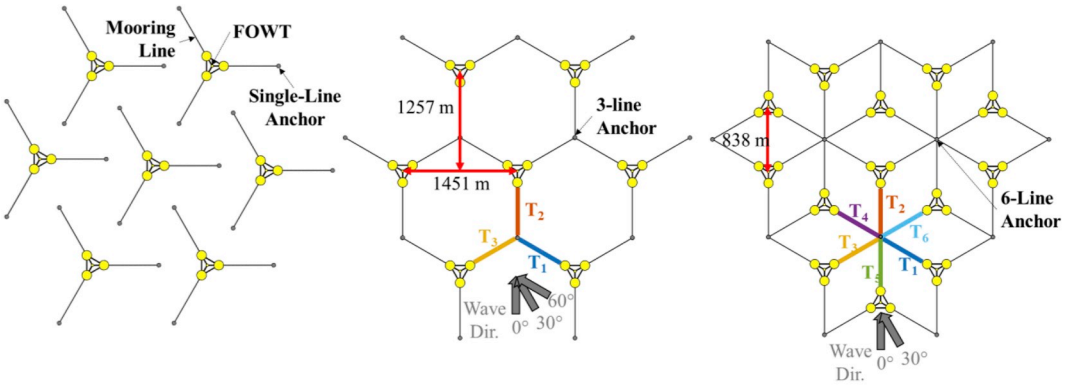

Fig. 2. Layout of a.) single-line, b.) 3-line and c.) 6-line anchor system for FOWTs. Scale is consistent across all images.

need to examine whether the spatial coherence of the waves in the multiline system affects the anchor forces significantly, compared to the configuration of the turbines in Fig. 2a where each anchor's load depends only on the dynamics of a single FOWT.

To determine the net force on an anchor being loaded by multiple mooring lines simultaneously, simulations of single-line FOWTs are completed, then post-processed as shown in Fig. 3. The net multiline anchor force is computed by the vector sum of the contributing single-line tensions. Since the mooring system is catenary, the contributing mooring lines tensions – T1, T2, and T3 - are purely horizontal (parallel with the seabed), therefore the resultant force on the multiline anchor – Tmulti – is also horizonal. Furthermore, anchors are modeled as fixed points at the seabed surface in FAST, therefore anchor characteristics like geometry and embedment depth are not relevant in this study.

It can be observed that the magnitude and direction of the net multiline anchor force is a function of the contributing line tensions. The net multiline anchor force is controlled by the maximum contributing (critical) single-line tension, while the smaller (cancelling) tensions, create a reduction in this force. This is where wave coherence between connected turbines is most important, as the magnitude of this reduction depends on the timing of the cancellation tension relative to the critical tension.

2.2. Multiline anchor force with unidirectional regular waves

The goal of this section is to determine the differences between the net multiline anchor force produced under perfectly in-phase and out-of-phase regular wave loading on the connected platforms. In-phase loading refers to regular wave crests acting on the connected FOWT platforms simultaneously (Fig. 4a), and out of phase loading refers to wave crests and troughs acting on the connected platforms simultaneously (Fig. 4b). These two cases represent bounding/limiting realizations of the way that spatially coherent irregular waves may affect multiline anchor loads. Equation of the regular wave surface, η, in the time domain is

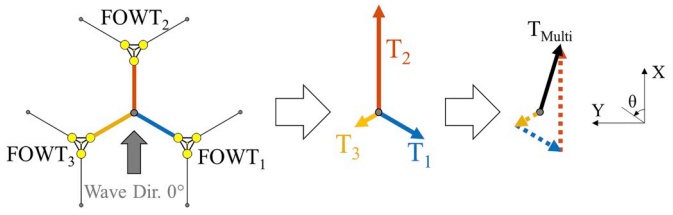

Fig. 3. Calculation of net multiline anchor force from contributing single-line tensions. Example shown for 3-line anchor system with 0° wave direction. θ is the direction of the waves.

$$\eta(x,t) = a\cos(kx - \omega t + \phi) \quad (1)$$

where k is wave number, x is distance, ω is wave frequency, t is time, a is regular wave amplitude ($H/2$) and ϕ is the random phase. For simplification in describing the effects of wave phase relative to line tension and anchor force, the following analysis focuses only on the 3-line anchor system. Fig. 4 reveals how the timing of the cancellation tension relative to the critical tension affects the cycle amplitude and maximum of the net multiline anchor force. It should be noted that wind forces are not included in Fig. 4, but will be incorporated later in this section.

To better understand these cases, the dynamics of the FOWT mooring system must first be examined. Wave elevation, platform displacement, and line tension are all tightly correlated. When a wave strikes and displaces a FOWT platform in its direction of travel, the upwind line (T_2) experiences peak tension, while the downwind lines (T_1 and T_3) simultaneously experience a minimum tension. Conversely, when a wave trough comes in contact, the platform displaces opposite the wave direction of travel, and in effect the upwind line (T_2) experiences a minimum tension while the downwind lines (T_1 and T_3) experience peak tensions. It should be noted however that these are general descriptions of the temporal relationship between wave strike, platform displacement (surge, heave, pitch), and line tension, as there can be significant and varying time delays between these events depending on the wave characteristics and the shape of the floating platform. Fig. 4a is a specific example in which there is negligible time delay, and the peak & minimum tensions are nearly simultaneous with the wave strike on the platform.

When critical and cancelling contributing tensions are out-of-phase, the amplitude and maximum of the net multiline anchor force are maximized (Fig. 4a). Conversely, when the critical and cancelling single-line tensions are in phase, the amplitude and maximum of the net multiline anchor force is minimized (Fig. 4b). This behavior is related to interference, in that waves in-phase at the connected platforms produce contributing line tensions with constructive interference, while waves out-of-phase at the connected platforms produces contributing line tensions with destructive interference.

Spatial characteristics, namely wavelength, are not considered in this step because it is not possible to compare the same wave acting on the connected platforms in both an in-phase and out-of-phase scenario when spacing between the FOWTs is held constant. In order to produce perfectly in-phase and out-of-phase wave loading of a certain wave height on the set of platforms in a multiline system, the waves would need to have slightly different wavelengths and periods; a wave train with N waves over a distance of 1257 m (see Fig. 2b) is different than a wave train with N+½ waves over the same distance. For example, a 6 m regular in-phase wave (i.e. 10 waves between the platforms) has a wavelength of 125.7 m and a wave period of 8.97 s. In contrast, a 6 m

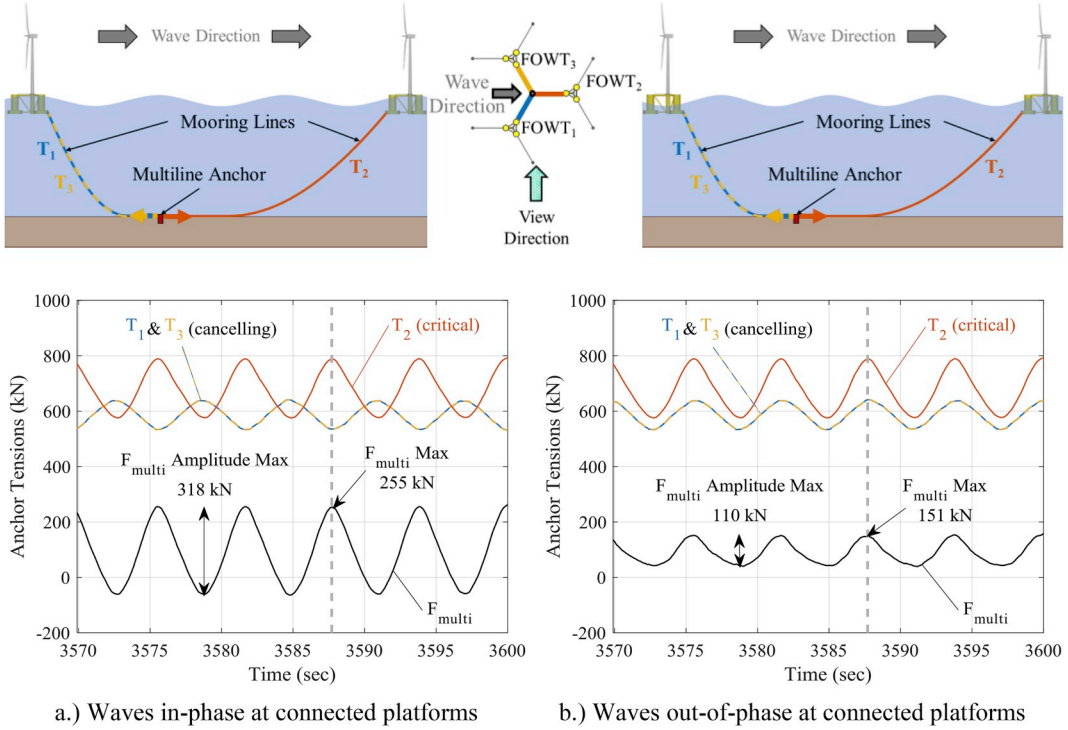

Fig. 4. Steady-state time history of contributing single-line tensions and net multiline anchor force for a.) in-phase wave loading and b.) out-of-phase wave loading. Example time histories are shown for 3 m regular waves with a period of 6.1 s and 0° wave direction. The wave height and length in the top figures are not to scale, so as to better exhibit wave phases. T_1, T_2, and T_3 are the contributing single-line tensions on the multiline anchor, and F_{multi} is the net multiline anchor force.

regular out-of-phase wave (10.5 waves between the platforms) has a wavelength of 119.7 m and a wave period of 8.75 s. Wavelength is determined by converting wave period to angular frequency, then using angular frequency and the water depth of 200 m in the linear dispersion relationship (DNV, 2007) to determine wave number k and in effect, wavelength.

Instead, the steady-state minima and maxima of the line tensions produced under regular wave loading are used to examine the magnitude of the anchor force produced by different sized regular waves. More specifically, the regular wave scenario is used here to evaluate the question where given a sea state (regular wave height), what is the best (minimum) and worst (maximum) loading on the multiline anchor. The minimum and maximum values of the maximum net multiline anchor force for all wave loading cases (Fig. 5) are found by offsetting the time between the critical and cancelling line tensions such that the maximum critical and minimum cancelling tensions are aligned in time (in-phase waves at the platforms), or the maximum critical and maximum cancelling tensions are aligned (out-of-phase waves at the platforms), as previously shown in Fig. 4.

The effect of wave phase at the platforms is examined over a range of wave heights and periods. In this context, wave period factor, t_f, is a value used in calculating wave period, given by

$$T = t_f \sqrt{H/g} \tag{2}$$

where T is wave period, H is wave height and g is gravity. Values of 11 and 14 for t_f are chosen to be close to the lower and upper bounds of this value as recommended in IEC 61400 (2009). Furthermore, the 0° wave direction is used for the entirety of this section because it is the most critical load direction case, meaning that it produces larger maximum single line and multiline anchor forces than those of the 30° and 60° case. Therefore, it is of the most interest relative to the effects of wave phases. Results are shown in Fig. 5.

In general, the range/variance of the net multiline anchor force relative to wave phase at connected platforms increases with wave height. The local maxima of anchor force that occurs at the 5 m wave height for $t_f = 11$ ($T = 7.9$ s) and at the 3 m wave height for $t_f = 11$ ($T = 7.7$ s) is due to the mean drift of the platforms. This mean drift force results from closeness of these wave frequencies to the rigid-body motion natural frequencies for the semisubmersible and its mooring system. Details on mean drift forces in the NREL semisubmersible floating system can be found in Coulling et al. (2013). The mean drift (or mean surge) displaces the platform in the direction of the waves, resulting on a higher mean tension on the critical line (T_2), and a lower tension on the cancelling lines (T_1 and T_3). It is this higher mean tension in critical line T_2 that amplifies on the maximum force for the wave periods close to the platform's rigid body motion natural frequency.

Similar trends are present for cases where the turbine is operating with the addition of a steady rated wind of 11.4 m/s and a steady current of 0.3 m/s in addition to regular waves, as shown in Fig. 6. Wind and current are modeled as co-directional with waves, and misalignment of the environmental loads may yield different results. It should also be noted that wind and currents change the wave characteristics for nonlinear interactions, which also affects the following conclusions.

The primary distinction of these operational cases compared to the wave-only cases is a smaller range/variance of the net multiline anchor force relative to wave phase at connected platforms increases with wave height. There is less sensitivity to wave phase differences in these operational cases because a significant portion of the line tension is being controlled by the wind loading, therefore changes in the wave phase have less effect. This is an important distinction to make over the non-operational wave-only scenario, as these larger values of anchor force are produced from a more realistic environmental conditions, and are likely closer to design values.

Anchor design is based primarily on a maximum anchor force (American Bureau of Shipping, 2014). Therefore, in this set of analyses, the difference in maximum net multiline anchor force between in-phase and out-of-phase wave loading can be thought of a measure of uncertainty in anchor demand. Anchor design uses whichever load case produces the largest anchor force, therefore it can be observed from the

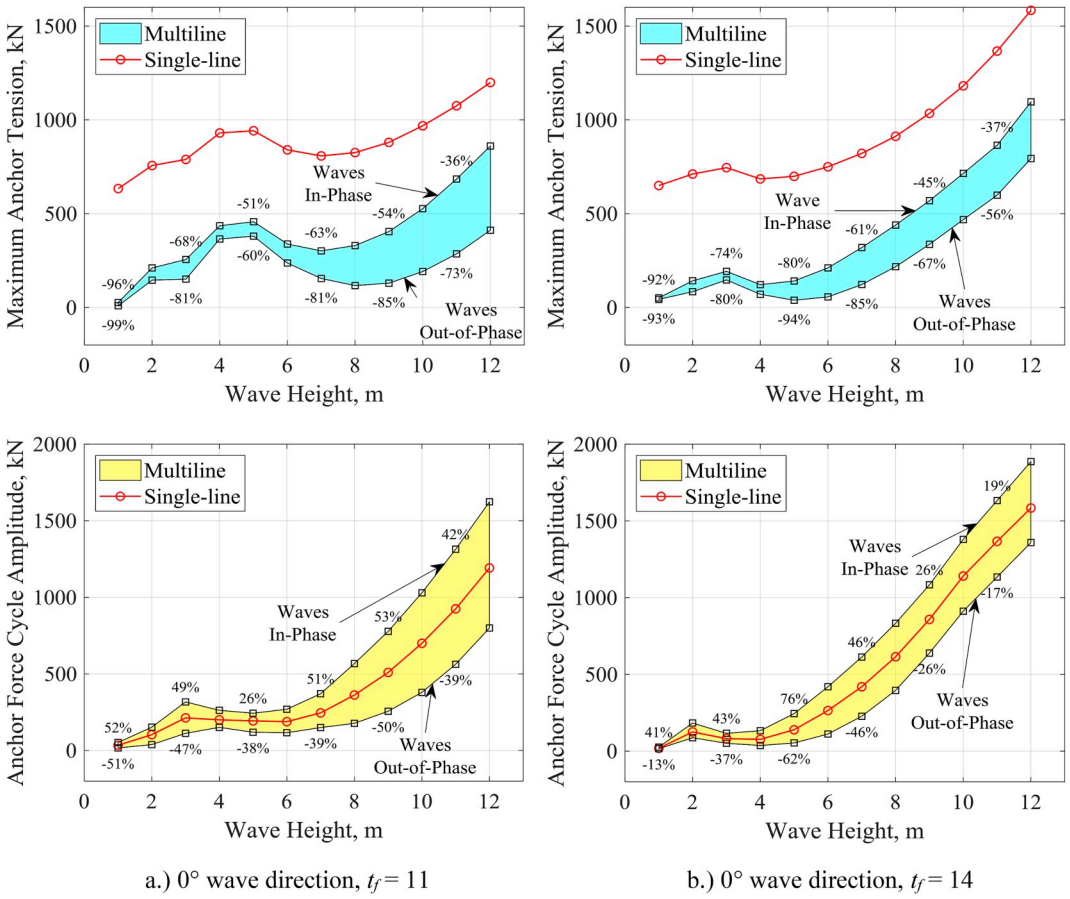

Fig. 5. Maximum multiline anchor forces and force cycle amplitudes under regular waves acting on parked and feathered FOWTs (no wind). Results show critical single-line (T_2) and net multiline anchor force versus regular wave height for a.) 0° wave direction and $t_f = 11$, and b.) 0° wave direction and $t_f = 14$, with percent difference from the critical single-line value shown. The upper bound corresponds to roughly in-phase waves at the connected platforms (Fig. 4a), the lower bound corresponds to roughly out-of-phase waves at the connected platforms (Fig. 4b), and the colored fill between them indicates the range in values over the wave phase difference at the connected platforms.

values in Figs. 5 and 6 that the larger wave height cases encompass the conditions most likely to control anchor design. These larger wave height cases see larger differences between maxima produced by in-phase and out-of-phase wave loading, which would potentially lead to a more conservative anchor design if irregular spatial wave coherence were to be deemed important.

The amplitudes of the anchor force cycles are used primarily in checking the fatigue strength of the anchor, and the smaller wave height cases encompass the conditions most likely to be used in fatigue analysis. Since the difference between in-phase and out-of-phase force cycle amplitude values are smallest in these small wave height cases, it can be anticipated that spatial wave coherence will not have a significant impact on fatigue analysis, even if irregular spatial wave coherence were to be deemed important.

While the force cycle amplitudes in larger (extreme) wave height conditions are not likely to be used in a fatigue analysis of the anchor, the bounds are still important in the context of anchor force direction reversal. This behavior can be seen in Fig. 4, where correlated loading produces a net multiline anchor force that reverses direction (min (F_{multi}) = −62 kN), while the anti-correlated loading does not (min (F_{multi}) = +42 kN). This behavior is of interest because force direction reversal is a characteristic of anchor loading that is not present in single-line anchors, which are only loaded in one direction. The effect of this force direction reversal within a single force cycle relative to anchor design is not yet known, as anchor design standards currently only apply to single-line anchors. This type of anchor loading event has been examined in previous work by the authors, which determined that multiline anchors can experience force direction reversal within a single cycle for extreme loading conditions (Fontana et al., 2017). It should be noted that force direction reversal falls within the broader topic of multidirectionality of the anchor force, which is an ongoing topic of study for the novel multiline anchor concept.

2.3. *Multiline anchor force with unidirectional irregular waves*

This section extends the previous section to the case of irregular unidirectional waves and seeks to understand how the multiline anchor force is affected by the use of spatially coherent irregular waves at connected platforms. The irregular waves in this study are modeled via the procedures outlined in Agarwal and Manuel (2010). They are linear, with a JONSWAP spectrum, and Rayleigh-distributed wave heights. All of the cases in this paper have been analyzed using first order kinematics with second order forces. The authors chose the first order kinematics due to the ease of calculating the closed form solution of wave propagation over the distance of the wind turbines, and because the default method of calculating second order kinematics in the FAST program used artificially adds energy to the wave spectrum to account for 2nd order effects. The authors believe that 2nd order kinematics will have little effect. In other words, first-order wave kinematics are used in the strip-theory solution, whereas the potential-flow solution is based on second-order theory.

Fourier coefficients for sea surface elevation, X, are

$$X(\omega_m) = A_m \exp(-i\phi_m) \tag{3}$$

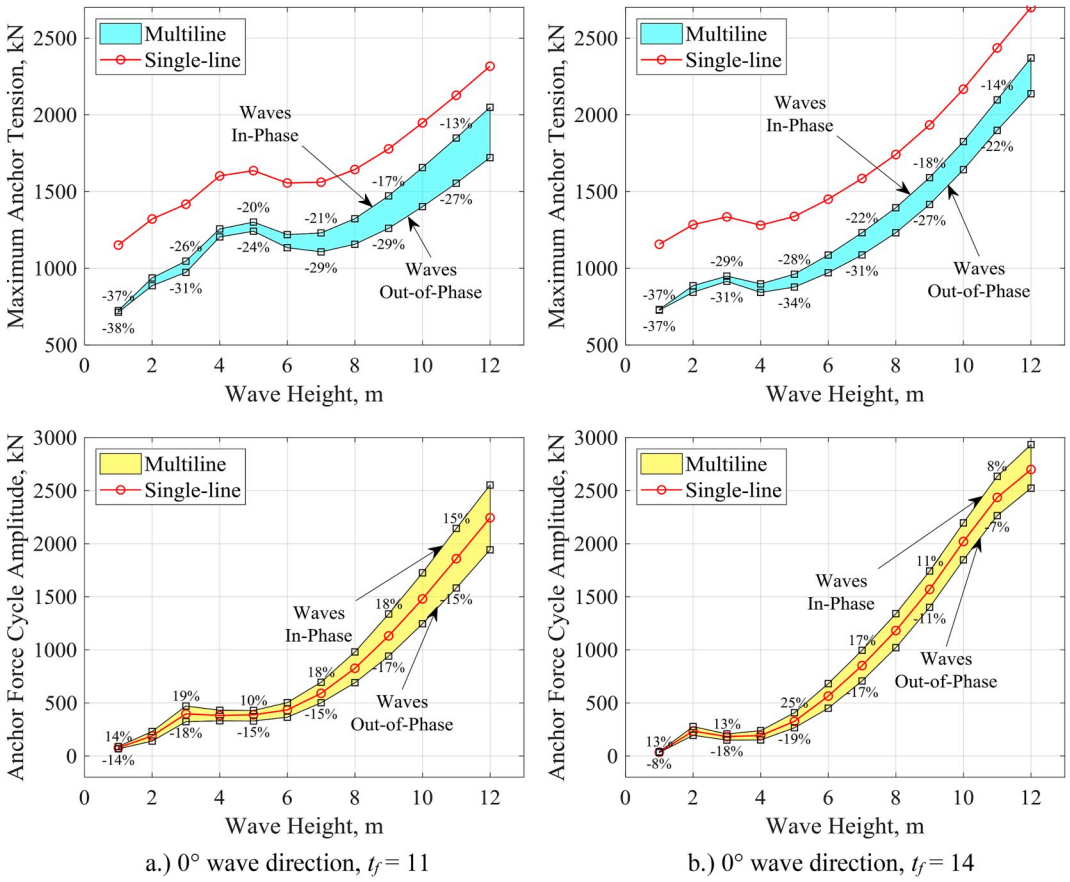

Fig. 6. Maximum anchor forces and anchor force cycle amplitudes under regular waves, steady wind (11.4 m/s), and steady current (0.3 m/s). Results show critical single-line (T_2) and net multiline anchor force versus regular wave height for a.) 0° wave direction and $t_f = 11$, and b.) 0° wave direction and $t_f = 14$, with percent difference from the critical single-line value shown. The upper bound corresponds to roughly in-phase waves at the connected platforms (Fig. 4a), the lower bound corresponds to roughly out-of-phase waves at the connected platforms (Fig. 4b), and the colored fill between them indicates the range in values over the wave phase difference at the connected platforms.

Where A_m is the Rayleigh distributed amplitudes and ϕ_m is the phase shift of frequency component m. The spatial phase shift is accounted for using the dispersion relationship at each frequency, given as

$$X(\omega_m) = A_m \exp(kx - i\phi_m) \tag{4}$$

In the final step, Fourier coefficients are transformed to the time domain to obtain the wave surface, resulting in

$$\eta(t,x) = \Re\{IFFT[X(\omega_m, \phi_m, x)]\} \tag{5}$$

This method of modeling creates time histories of unidirectional spatially coherent waves over a distance (Sarpkaya and Isaacson, 1981). When they are applied to the FOWT simulations, the variation in wave elevation is spanned only over the direction of travel, and wave elevation is identical over the direction perpendicular to their travel due to the unidirectional nature, as shown in Fig. 7.

With this use of unidirectional wave fields, multiple turbines connected to the multiline anchor experience identical wave loading under spatially coherent wave conditions. This is shown in Fig. 8a for Turbines 1 and 3, and Fig. 8c for Turbines 2 and 3. More specifically, the only scenario in which duplication of wave elevation time history at two turbines does not occur is for the 3-line anchor with 30° wave direction. Therefore, this case is focused on more specifically in the following analysis, although the other cases are discussed as well. Where there is wave loading duplication in the coherent case due to location (Turbines 1 and 3 in 0° degree, Turbines 2 and 3 in 60° direction), the corresponding independent wave loading case also uses 2 of the same, although independent, waves fields at these turbines for consistency in comparison (See Fig. 8a and c).

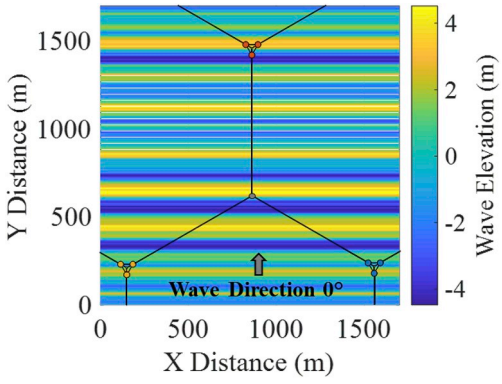

Fig. 7. Unidirectional irregular wave field traveling in 0° direction in 3-line anchor system for $H_s = 8$ m and $t_f = 14$.

In this section, the coherent wave condition refers to simulations of the net multiline anchor force in which the connected turbines are loaded by spatially coherent waves, where wave elevation time history at the distance location of each turbine is generated via the procedure outlined in Equations (1) and (3) through (5). The independent wave condition refers to simulations of the net multiline anchor force in which the connected turbines are loaded by independent waves. The independent cases shown in Fig. 8 assume that the waves are long-crested, such that the wave profiles are identical between T1 and T3 for the

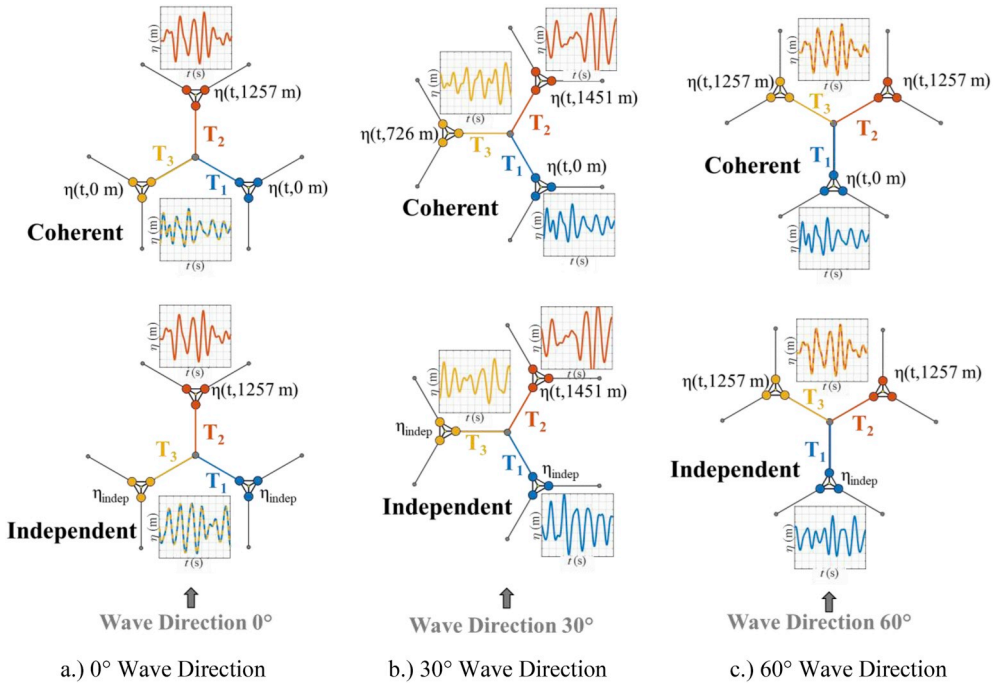

Fig. 8. Description of wave elevations for a.) 0° wave direction, b.) 30° wave direction, and c.) 60° wave direction.

0° wave direction case, and between T3 and T2 in the 60° degree case, but whose random phase shifts, ϕ, are independent from the other turbines. For the coherent case, the waves are again long-crested, but the phase angles, ϕ, are identical for all 3 turbines. To make the comparison between coherent and independent wave conditions easier for each wave direction, the wave history that generates the critical contributing line tension T_2 remains common, while cancelling tensions T_1 and T_3 are changed to fit the degree of wave coherence (see Fig. 8). This was done to remove a source of variation between different realizations of a wave field that is not related to coherence. As a result, the wave elevation at Turbine 1 locations (x = 0 m) is not the same across different wave directions, but wave elevation is identical at turbine locations that produce governing contributing tensions T2 (x = 1257 for wave directions = 0° and 60°, and x = 1451 m for wave direction = 30°). The contributing line tensions and the net multiline anchor force for the coherent and independent case can be seen in Fig. 9. Fig. 9 also displays how the dominant contributing force of T_2 controls the behavior of the net multiline anchor force. For each combination of significant wave height, wave period factor, direction, and coherence or independence, six realizations were completed, consistent with the number of realizations recommended by IEC for design (IEC 61400-3, 2009).

The effect of wave coherence is examined for both the 3-line and 6-line geometries, as shown in Fig. 2. The difference in the multiline anchor force dynamics between the coherent and independent wave conditions is shown in Table 1, and which shows average values across the six realizations. The percent difference in the maximum value, mean value, and standard deviation of the net multiline anchor force for coherent and independent waves is calculated relative to the corresponding T_2 single line value. The maximum significant wave height is chosen based on Survival Load Case (SLC) conditions of the full-scale VolturnUS, a planned floating wind demonstration project in the Gulf of Maine (Viselli et al., 2016). It should be noted that the 0 values in Table 1 are not absolute 0 values, but rather a result of rounding values < 0.5 to one significant digit. Percent difference in Table 1 is calculated by

$$\%\ difference = 100 * \frac{V_{MC} - V_{MI}}{V_S} \tag{6}$$

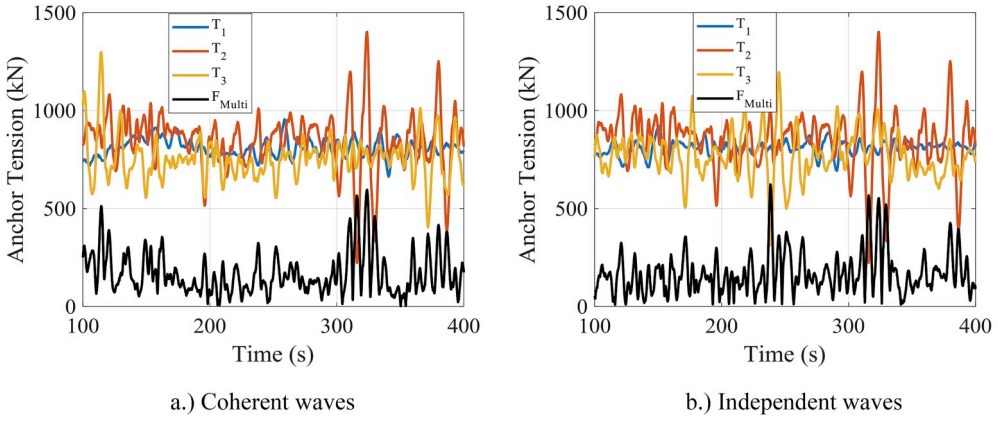

Fig. 9. Time history snapshot of contributing line tensions and net multiline anchor force for $H_s = 8$ m, $t_f = 14$, and wave direction = 30° for a.) coherent and b.) independent waves.

Table 1
Percent difference between coherent and independent value of net multiline anchor force, relative to T_2 single-line value. The intensity of shading reflects the magnitude of the percent difference for each value in question – maximum, mean, and standard deviation.

		3-Line Anchor									6-Line Anchor					
		0° Dir.			30° Dir.			60° Dir.			0° Dir.			30° Dir.		
		H_s (m)			H_s (m)			H_s (m)			H_s (m)			H_s (m)		
		4	8	12	4	8	12	4	8	12	4	8	12	4	8	12
Maximum	11	2	4	0	3	-4	4	1	5	-2	-8	0	4	9	-11	9
(t_f (%))	14	0	1	-1	1	5	0	2	0	1	-2	0	8	2	12	-1
Mean	11	0	0	0	0	0	0	0	0	0	-1	0	2	1	0	0
(t_f (%))	14	0	0	0	0	0	0	0	0	0	0	0	5	0	0	0
Standard Deviation	11	1	0	0	8	1	0	5	-1	2	-10	-5	2	18	1	0
(t_f (%))	14	0	0	0	3	0	0	0	1	0	-9	-3	6	7	-1	0

where V_{MC} is the value of the multiline anchor force with spatially coherent wave loading, V_{MI} is the value of the multiline anchor force with independent wave loading, and V_S is the maximum contributing single-line anchor force (T2), which is the same for multiline anchors with both coherent and independent wave loading.

The lack of any consistent trend in the differences for the net multiline anchor force suggest that the differences result primarily from natural randomness of the irregular wave fields, not from a difference in coherence versus regular wave loading. This lack of any trend was further confirmed by adding 6 additional irregular wave realizations, for a total of 12 realizations to be averaged across. Larger differences are seen in the 6-line anchor cases, as the duplicate wave effects are amplified by the presence of additional line attachments.

When examining multiline anchors forces, one of the most distinctive characteristics is the directionality of the force. In a single-line anchor system, only one mooring line is attached, therefore the anchor is loaded in one direction that varies by less than 1° for the OC4 floating system in any of the simulations completed. In a multiline anchor system, multiple mooring lines are attached, and the anchor is loaded in many different directions with many different force magnitudes. Therefore, a comparison must be made of the directionality of the net multiline anchor force between the coherent and independent wave conditions, as shown in Table 2. This comparison is only shown for the 30° wave direction, because the duplicate wave effect renders the anchor force directionality for the other wave directions unidirectional - the direction of the net multiline anchor force in the 0° and 60° wave direction cases in the 3-line anchor system and the 0° and 30° wave direction cases in the 6-line anchor system fluctuate between the positive and negative value of the wave direction. Due to the exact symmetry of the loading in the direction perpendicular to the waves, y-components (y-direction being perpendicular to wave direction) of the contributing tensions cancel out perfectly due to the duplicate wave effect, therefore the direction of the multiline anchor force only varies back and forth in the exact direction of the waves. For the 30° wave direction case, which does not have any duplicate wave effects, the variation in the direction of the multiline force can be seen in Fig. 10.

As with Table 1, the lack of any consistent trend in the differences for the mean and standard deviation of the net multiline anchor force direction suggests that the differences result primarily from natural

Table 2
Value difference of mean and standard deviation of direction of net multiline anchor force between coherent and independent conditions. The intensity of shading reflects the magnitude of the difference in value.

		Wave H_s (m)					
		2	4	6	8	10	12
Difference in Mean Direction of Net Multiline Anchor Force (°)	11	3	-2	-1	0	2	0
	12	4	-2	0	1	0	2
(t_f)	13	3	0	0	1	1	0
	14	2	0	1	1	1	2

		Wave H_s (m)					
		2	4	6	8	10	12
Difference in Standard Deviation Direction of Net Multiline Anchor Force (°)	11	-3	5	2	0	-1	0
	12	-4	4	2	-1	0	-1
(t_f)	13	-3	2	0	-1	-1	0
	14	-1	1	0	0	0	0

randomness of the wave fields. This lack of any trend was again confirmed by adding 6 additional irregular wave realizations, for a total of 12 realizations to be averaged across. The lack of difference between the coherent and independent wave cases is also exhibited in the rosettes. While some of the rosettes not shown here exhibit slightly larger differences in shapes, there is still no consistency or trend in these small differences. This further bolsters the conclusion that the differences are a product of the natural dissimilarity between two different realizations of waves, not a difference due to the use of spatially coherent waves versus independent waves.

The smallness of the differences in the critical values of the net multiline anchor force reveal that spatial wave coherence does not have any significant effect on the dynamics of the net multiline anchor force, and that assumption of independence of the wave fields at different

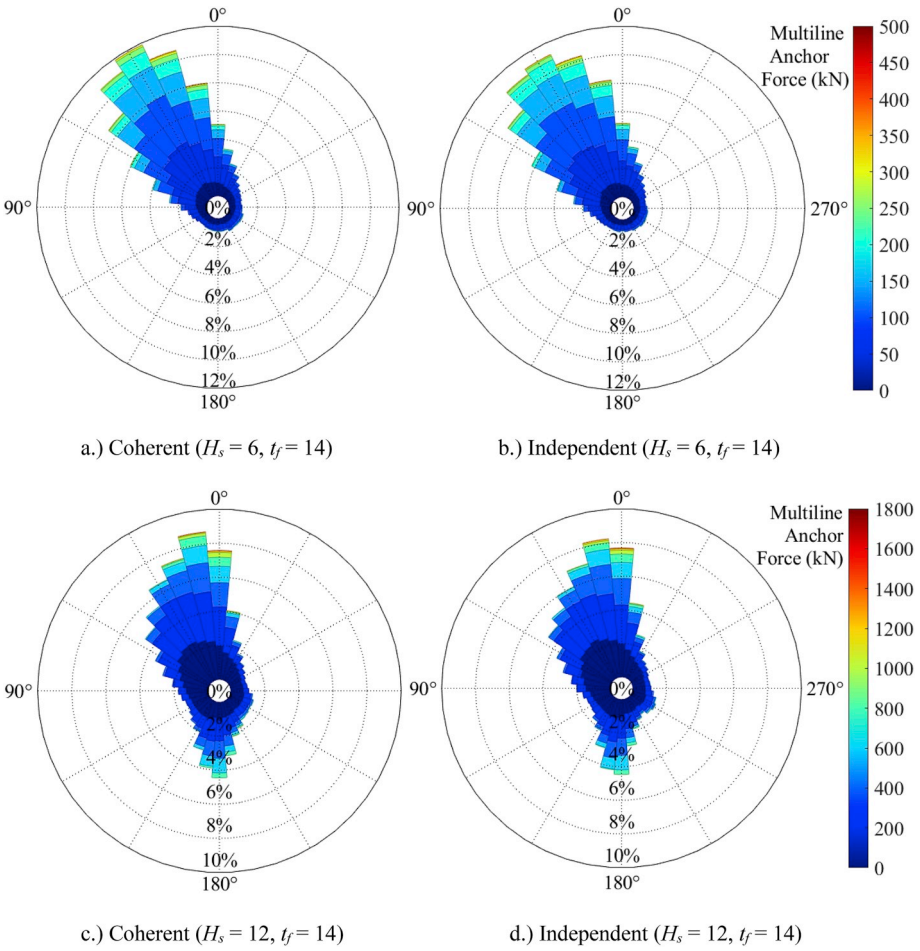

Fig. 10. Force direction rosettes for the net multiline anchor force in the 30° wave direction with $H_s = 6$ m and $t_f = 14$ for a.) coherent wave condition and b.) independent wave condition, and with $H_s = 12$ m and $t_f = 14$ for c.) coherent wave condition and d.) independent wave condition. Rosettes show binning of all the wave directions, and the percentage value in each directional bin shows frequency of occurrence.

FOWT locations provides sufficiently accurate anchor load characterizations. This conclusion is of course of quite a different nature than that of regular waves in Section 2.2, and this difference is explained in Section 3.

3. Wave coherence

The lack of difference between the coherent and independent wave results in the previous analysis suggests that wave coherence at connected turbines in a multiline anchor system is insignificant in determining multiline anchor force dynamics. The following section seeks to better understand and explain these results by focusing on only the waves and their characteristics and examining the distances at which wave elevations are no longer correlated enough to produce measurable synchronicity (or anti-synchronicity). The metric used here to determine the relationship of waves at different locations is the correlation coefficient between wave elevation time histories at different distances.

3.1. Regular waves

Before examining realistic irregular waves, the correlation of regular waves is first presented. A regular wave, in the shape of a repeating sine wave, is shown in Fig. 11.

The relationship between wave elevation and space is expressed through the correlation coefficient, R, which is a measure of the strength and direction (positive or negative) of the linear relationship between two variables. For regular waves, at intervals of the wavelength, the correlation coefficient is 1, and the wave elevations at a time lag of one wave period are perfectly correlated. Conversely, at intervals of wavelength plus or minus one half, the correlation coefficient is −1, and the wave elevations at these points are perfectly anti-correlated. These

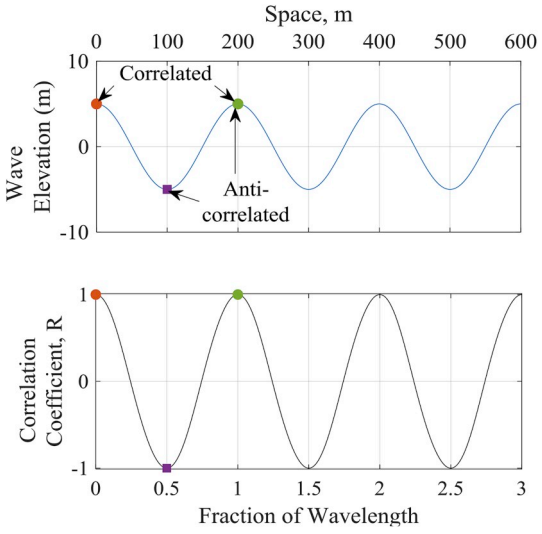

Fig. 11. Wave elevation and correlation coefficient of a regular wave train with wave height of 10 m and wavelength 200 m.

characteristics can be seen in Fig. 11, where the red and green markers are perfectly correlated, and the purple and green markers are perfectly anti-correlated. With regular waves, each wave has an identical height, length, and period, therefore the location of and time between any of the crests and troughs can be perfectly and infinitely identified. With irregular waves in the following analysis, R serves as a measure of predictability for the locations of the crests and troughs of the waves.

3.2. Unidirectional irregular waves

This section builds upon the previous section, with the goal of examining the correlation coefficient between irregular wave elevation time histories at different distances. Elevation time histories of irregular spatially coherent waves are generated via the procedures outlined in Equations (1) and (3) through (5), and each is generated over a distance of 7 peak spectral wavelengths for a 1-h duration. Sections of a sample time history are shown in Fig. 12.

Fig. 12b reveals more clearly how quickly a specific wave moves in space, and how long it lasts in time. The colored ridges correspond to specific waves and show that larger waves generally last longer and travel faster than smaller waves (yellow ridges compared to green ridges). It can be observed that even the largest waves are only able to maintain themselves in the wave train no more than several hundred meters, which is far less than any turbine spacings in Fig. 8.

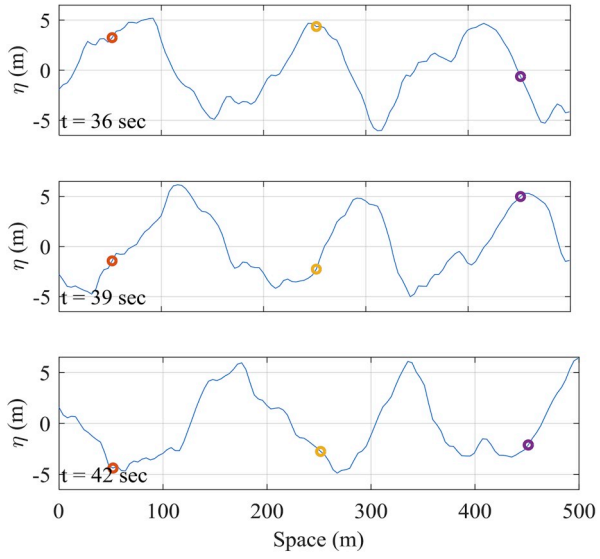

a.) Time snapshots of wave elevation in space

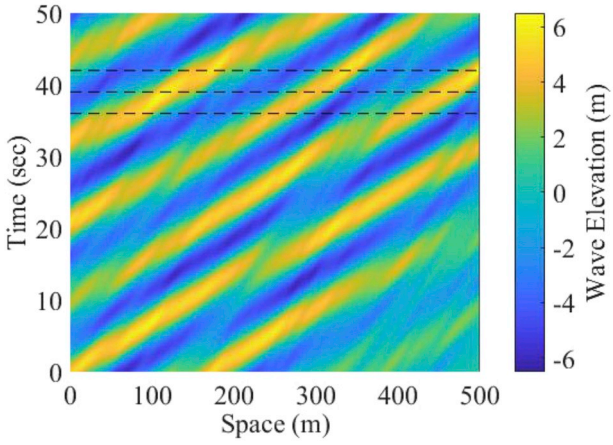

b.) Wave elevation versus space and time

Fig. 12. a.) Time snapshots of wave elevation over space generated for different time instances and b.) wave elevation versus space and time. Example shown for significant wave height of 10 m, peak spectral wave period 11.3 s, and peak spectral wavelength 200 m in water depth of 200 m. The markers in a.) are separated by a distance of 1 peak spectral wavelength, or 200 m. The three subfigures in a.) correspond to the three dashed lines in b.).

Wave correlation relative to space and time can be calculated by

$$R(x) = \frac{cov(\eta(t,0),\eta(t,x))}{\sigma_{\eta(t,0)} \times \sigma_{\eta(t,x)}} \tag{7}$$

where R is the correlation coefficient of wave time histories at locations 0 and x, x is distance, t is time, η is wave elevation, σ is standard deviation, and cov is covariance. The correlation coefficient with distance is shown in Fig. 13. It is important to note that the correlation coefficient is used over the space domain, as the interest lies in how wave elevation time histories at different locations correlate, not how a single wave propagates over time. Fig. 13a shows the correlation coefficient of waves generated with the minimum recommended period, and Fig. 13b shows waves generated with the maximum recommended period as designated by IEC offshore wind turbine design standards (IEC 61400-3, 2009). The relationship of correlation coefficient with distance is averaged across 18 realizations of the random process for each combination of significant wave height and peak spectral wave period.

Similar to the regular waves, the correlation coefficient function still experiences peaks at intervals of peak spectral wavelength, but the magnitudes of the peaks decay with distance due to irregularity and loss of correlation of the wave train. These peaks at intervals of peak spectral wavelength are used to fit an exponential decay function, as shown in Fig. 14. The decay constant, C_d, measures how quickly the correlation coefficient approaches 0. This relationship is determined relative to distance (Fig. 14) rather than fraction of peak spectral wavelengths (Fig. 13) to allow for comparisons of C_d across different wave parameters. Correlation length, x_c, is defined as the distance x at which the correlation coefficient is equal to e^{-1}, or 0.368. A large decay constant means that the correlation coefficient decreases quickly (short correlation length), and a small decay constant means the correlation coefficient decreases slowly (long correlation length).

This relationship can be expressed by

$$R(x) = exp(-C_d x) \quad for \quad x = \lambda n \tag{8}$$

where R is the correlation coefficient between the wave elevation time history at a starting point and a wave elevation time history at a point n peak spectral wavelengths away, x is distance from the starting point, C_d is decay constant, n is an integer, and λ is peak spectral wavelength.

A parametric study reveals how wave height (H_s), wave period factor (t_f), and water depth affect decay constant and in effect, correlation length. Parameter ranges are given in Table 3. Wave period factors (t_f) extend slightly beyond the recommended range of 11.1–14.3 given in IEC 61400 (2009) for modeling normal and extreme wave heights.

The relationship between input wave parameters and the correlation length can be seen in Fig. 15.

In general, it can be seen that wave correlation length increases with significant wave height. Water depth has a very small effect on the relationship between correlation length and wave characteristics. The correlation length is largely independent of changes in wave period factor, except for very large wave heights. The maximum correlation length of 298 m occurs for water depth = 50 m, t_f = 11.5, and H_s = 12 m, where C_d = 0.0034. The minimum correlation length of 16 m occurs for H_s = 1 m and t_f = 10 for all water depths, where C_d = 0.0639.

Referring back to the multiline anchor analysis, for the maximum significant wave height of H_s = 12 m with t_f = 11 and water depth = 200 m, the minimum decay constant is 0.0042 and the maximum correlation length is 238 m. This correlation length is significantly smaller than any of the minimum turbine spacings in the multiline anchor layouts, as shown in Table 4.

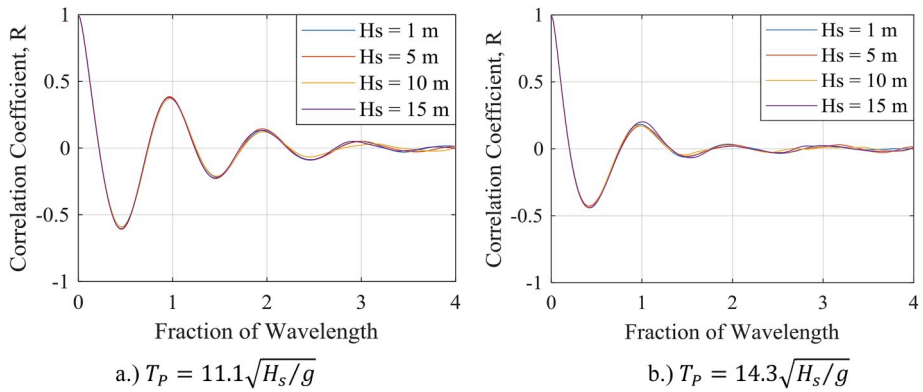

Fig. 13. Correlation coefficient of irregular waves with space relative to number of peak spectral wavelengths for a.) minimum recommended peak spectral period and b.) maximum recommended peak spectral period.

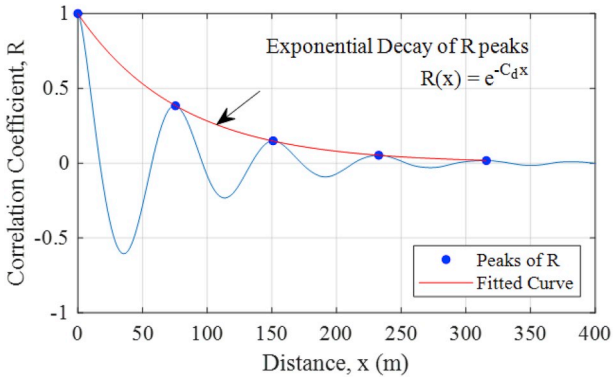

Fig. 14. Exponential decay function fit for water depth = 200 m, H_s = 4 m, t_f = 11, and peak spectral wavelength = 77 m. Decay constant, C_d, is 0.0127 m^{-1} and correlation length, x_c, is 79 m.

Table 3
Range of parameters for modeling spatially coherent irregular waves.

	Range	Step Size
Water Depth (m)	50–500	50
Significant Wave Height, H_s (m)	1–12	1
Wave Period Factor, t_f	10–15	0.5

These very low correlation coefficients (<0.2) supplement the conclusion that spatial coherence of the waves at these distances does not have any significant effect on the multiline anchor force compared to the independent wave scenario.

Directional waves were also investigated in this context of correlation length. Two dimensional wave spreading was assumed to follow the cosine spreading function, independent of wave frequency, and was implemented using the Seasim function in the WAFO toolbox in MATLAB. It was found that the correlation coefficient decays faster in the directional wave case than in the unidirectional wave case (Fig. 16), and as a result, wave correlation lengths are shorter in the directional case. Therefore, the use of unidirectional waves is a conservative choice in that, if there was any effect of spatial wave coherence on net multiline anchor force, it is expected that it would be revealed here. These unidirectional wave field results effectively allow the assumption that the directional wave field would also not result in any difference between spatially coherent and independent wave loading at platforms connected to a multiline anchor.

3.3. Minimum spacing of installed offshore wind turbines

The correlation lengths of this study are evaluated here in the context

Table 4
Correlation coefficient of waves at distances of minimum spacings in multiline configurations.

Multiline Configuration	Wave Direction (°)	Minimum Turbine Distance in Direction of Wave Travel (m)	Minimum Decay Constant	Wave Correlation Coefficient at Minimum Turbine Distance
3-line	0	1257	0.0042	0.005
	30	725		0.048
	60	1257		0.005
6-line	0	417		0.174
	30	725		0.048

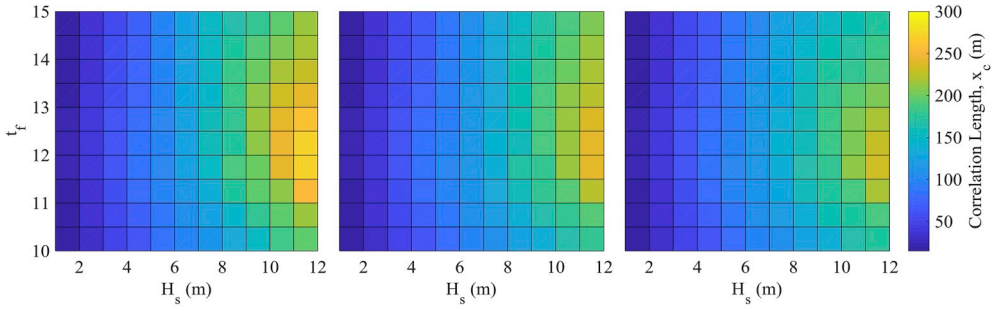

Fig. 15. Correlation length relative to wave parameters for a.) 50 m water depth, b.) 100 m water depth and c.) 500 m water depth.

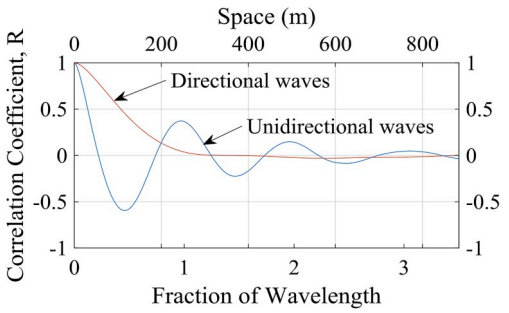

Fig. 16. Correlation coefficient decay for unidirectional and multidirectional waves. Example shown for $H_s = 12$ m, $t_f = 11.5$, and depth = 200 m, which are the conditions that produce the largest wave correlation lengths in this study.

of typical spacing between turbines in installed offshore wind farms. While there is only one operational floating offshore wind farm, observations can still be made for the many installed fixed-bottom wind farms. The following analysis of turbine spacing uses only wind farms that employ turbines with a 4 MW or greater capacity, as deployment of commercial-scale floating wind technologies is likely to coincide with the progression to larger turbines (Spyroudi, 2016). The wind farms from this study exhibit a range of turbine capacities, farm sizes, and countries of origin, and all wind farms were commissioned within the past 10 years. It was found that most of the installed wind farms in this study have minimum turbine spacings between 4 and 8 rotor diameters, with fixed bottom wind turbine spacings ranging from 435 to 1072 m (see Fig. 17). Data for this study was obtained from 4C Global Offshore Wind Farms Database (2018), and details on the determination of turbine minimum spacings can be found in the Appendix.

The first and only floating offshore wind farm as of writing this paper, Hywind Pilot Park (Statoil, 2016), employs the largest turbine spacing by a significant amount in terms of both total distance and number of rotor diameters. While no conclusions can be drawn from this singular example of a floating offshore wind farm, it is still important to note the outlier nature of this point amongst the other offshore wind farms.

The most important conclusion to note is that the wave correlation lengths in Section 3.1 of this study (<300 m) are smaller than typical spacings of installed OWTs (>500 m), and anticipated spacings of other FOWTs. Even if the significant wave height in the correlation length study is increased to 18 m, the maximum correlation length is only 413 m, which is still smaller than any of the current spacings of most installed offshore wind farms using 4 MW or larger turbines.

The idea of changing the mooring system and/or wave characteristics such that turbine spacings were less than or equal to the wave correlation length was considered. However, this was not realistic. From extrapolating the relationship between maximum correlation length and significant wave height in 200 m water depth, it was estimated that unrealistically large significant wave heights ($H_s > 25$ m, more than double the SLC value of H_s in the full-scale VolturnUS (Viselli et al., 2016)) would be needed to create correlation lengths greater than the minimum turbine spacing in terms of rotor diameter of any currently installed offshore wind farms (Rotor Diameter = 126 m, RD = 4.0, Spacing = 504 m).

4. Conclusions

This paper investigated spatial characteristics of linear waves in the context of a multiline anchor system for floating wind turbines. The goal was to determine if multiline anchor force dynamics are a function of spatial wave coherence, or if the treatment of wave fields as independent at each turbine provides adequate load characterizations. While regular waves fields in the multiline system showed the limits of what the difference in multiline anchor forces could be between these two models

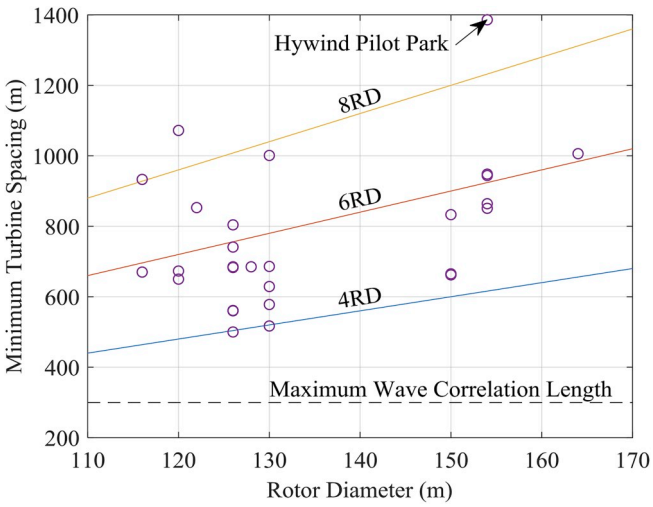

Fig. 17. Turbine rotor diameter versus minimum turbine spacing for installed offshore wind farms.

could be, the irregular wave fields applied to FOWTs in a multiline anchor system revealed no consistent trends that differentiated multiline anchor force dynamics generated by spatially independent versus coherent waves. Differences between the two wave loading models were insignificant – mean anchor force values differed by less than 1% and maximum anchor force values differed by less than 5% in the 3-line anchor system. A deeper investigation into spatial wave characteristics revealed that the correlation coefficient between wave elevation time histories at different points in space decays rapidly with distance between the points. Even for the maximum wave height studied ($H_s = 12$ m), the correlation length was less than 300 m.

The situation where wave coherence could potentially have an effect on multiline anchor force dynamics is one in which turbine spacing is less than or equal to wave correlation length. It is almost certain that this situation is not feasible/possible for several reasons. First, in the context of turbine spacing, it is observed that spacing will likely not be less than 4 rotor diameters. This minimum spacing limit, coupled with the limit of floating turbines not being less than 4 MW capacity and 120 m rotor diameter, means that the absolute minimum spacing of FOWTs is likely to be at about 500 m. In combination with the findings in Section 3.2 that significant wave heights must be unrealistically large ($H_s > 25$ m) to produce wave correlation lengths of this distance, it can be concluded that a situation will not exist in which waves will be significantly correlated at the connected platforms in multiline anchor systems for FOWTs. It should be noted that this analysis is fundamentally linear and based on simple superposition. For non-linear waves, the correlation and the maximum loads might be different. This study is considering the effect of rather large and long waves, intrinsically non-linear, particularly the asymmetry of the free surface and the velocity profile, thus the force time series at the mooring lines will be significantly affected. Therefore the conclusions are only valid for linear wave systems.

Funding sources

This work was supported by the US National Science Foundation [grant numbers IGERT-1068864, CMMI-1463273, CMMI-1463431, and CMMI-1462600], and the Massachusetts Clean Energy Center.

Declarations of interest

None.

Acknowledgements

This work is generously funded by US National Science Foundation grants IGERT-1068864, CMMI-1463273, CMMI-1463431, and CMMI-1462600 and the Massachusetts Clean Energy Center.

Appendix A. Supplementary data

Supplementary data to this article can be found online at https://doi.org/10.1016/j.oceaneng.2019.04.048.

Appendix

Minimum turbine spacings were determined from Matlab image processing procedures, with images of offshore wind turbine locations taken from the 4C Offshore resource (4C Offshore, 2018). This is a public resource that provides a large amount of information about offshore wind farms. The map feature of this resource provides the location and layout of many fully commissioned offshore wind farms, as shown in Fig. 18.

The use of this resource allows for the determination of turbine locations, and in effect, turbine spacings. The image in Fig. 18a is first converted into matrix form using the *imread* function, then turbine locations are obtained using the *imfindcircles* function. These initial turbine locations are in terms of pixel distances, and the map scale key provided in for each wind farm was used to determine the number of meters per pixel.

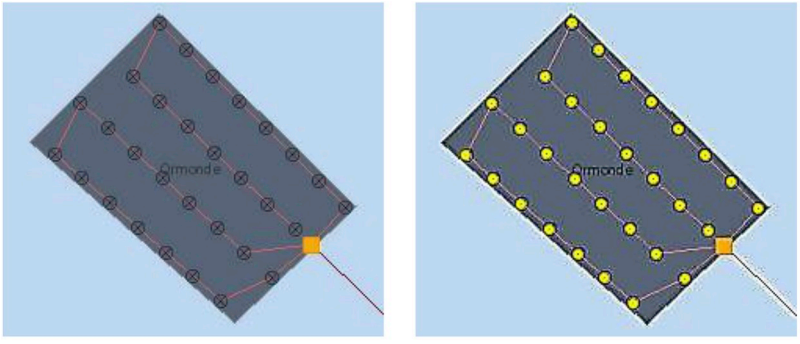

a.) Original image b.) Sharpened image with turbine locations

Fig. 18. Image processing of map data from 4coffshore to obtain turbine locations. The minimum distance for grid-layout farms such as Ormonde offshore wind farm in Fig. 18 is simple, but determining spacing for farms such as the Bard 1 Offshore Wind Farm in Fig. 19 is more complex.

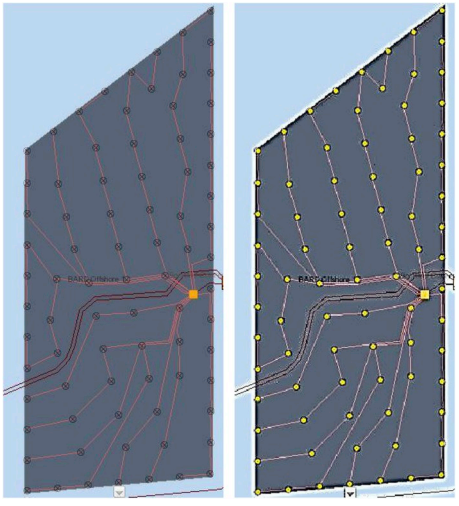

Fig. 19. Inconsistent turbine spacing in Bard Offshore 1 wind farm.

In cases such as this, where turbine layout lacks a pattern/grid and spacing is inconsistent, an alternate method is used to determine spacing. The Delanuay triangulation function in Matlab (*delaunayTriangulation*) is used to determine which turbines are the nearest neighbors for each turbine, and the distance of the nearest neighboring turbine in noted. The minimum spacing value for the farm is then taken as the average of these values for all turbines in the farm. Results for minimum turbine spacing are shown in Table 5. It should be noted that minimum turbine spacing in the context of wave coherence would depend on the WWC direction, therefore the calculation of the turbine spacings for the closest spaced turbines in a wind farm serves as a conservative estimate for this topic.

Table 5
Minimum turbine spacing of installed offshore wind farms. RD = spacing in terms the turbine rotor diameter. * indicates farms in which minimum turbine spacing was found in the literature. All others were calculated from the open-source map data on http://www.4coffshore.com/windfarms

Wind Farm	Year	Location	Turbine Capacity	Number of Turbines	Rotor Diameter	Minimum Turbine Spacing	RD
Alpha Ventus	2010	Germany	5	12	126	804	6.4
BARD Offshore 1	2013	Germany	5	80	122	853	7.0
Block Island Wind Farm	2017	U.S.	6	5	150	833	5.6
Borkhum Riffgrund 1	2015	Germany	4	78	120	673	5.6
Burbo Bank Extension	2017	U.K	8	32	164	1006	6.1
Dudgeon	2017	U.K.	6	67	154	851	5.5
Formosa	2017	Taiwan	4	2	120	1072	8.9
Fujian Putian City	2016	China	5	10	128	685	5.3
Gemini	2017	Netherlands	4	150	130	629	4.8
Global Tech I	2015	Germany	5	80	116	670	5.8
Gode Wind phases 1 + 2	2017	Germany	6	97	154	864	5.6
Hywind Pilot Park *(Statoil, 2015)	2017	Scotland	6	5	154	1386	9.0
Huaneng Rudong North	2017	China	5	34	150	662	4.4
Huaneng Rudong South	2017	China	4	36	150	665	4.4
London Array *(London Array Operations and Maintenance Base, n.d.)	2013	U.K.	3.6	175	120	650	5.4
Longyuan Putian Nanri	2015	China	4	4	130	517	4.0
Nordsee One *(Nordsee One GmbH, 2017)	2017	Germany	6.15	54	126	741	5.9
Nordsee Ost	2015	Germany	6.15	48	126	561	4.5
Ormonde *(Ormonde Development, 2005)	2012	U.K.	5.075	30	126	560	4.4
Race Bank	2018	U.K.	6	91	154	944	6.1
Sandbank1	2017	Germany	4	31	130	1001	7.7
SPIC Binhai North H1	2016	China	4	25	130	686	5.3
Tahkoluoto	2017	Finland	4	10	130	578	4.4
Thorntonbank I *(Peire et al., 2009)	2009	Belgium	5.075	6	126	500	4.0
Thorntonbank II	2013	Belgium	6.15	30	126	683	5.4
Thorntonbank III	2013	Belgium	6.15	18	126	685	5.4
Trianel Borkum I	2015	Germany	5	40	116	933	8.0
Westermost Rough	2015	U.K.	6	32	154	948	6.2

The wind farms that had literature containing spacing information were effective in verifying the image processing and turbine spacing calculation methods used for the majority of farms that do not publicly state minimum spacing values.

References

Agarwal, P., Manuel, L., 2010. Incorporating irregular nonlinear waves in coupled simulation of offshore wind turbines. In: 48th AIAA Aerospace Sciences Meeting Including the New Horizons Forum and Aerospace Exposition. https://doi.org/10.1016/j.apor.2011.02.001.

Alvise, B., Francesco, B., Filippo, B., Sandro, C., Mauro, S., 2017. Space-time extreme wind waves: analysis and prediction of shape and height. Ocean Model. 113, 201–216. https://doi.org/10.1016/j.ocemod.2017.03.010.

American Bureau of Shipping, 2014. Guide for Building and Classing Floating Offshore Wind Turbine Installations.

Balitsky, P., Fernandez, G.V., Stratigaki, V., Troch, P., 2017. Assessing the Impact on Power Production of WEC array separation distance in a wave farm using one-way coupling of a BEM solver and a wave propagation model. In: 12th European Wave and Tidal Energy Conference, pp. 1–10.

Carbon Trust, 2015. Floating Offshore Wind: Market and Technology Review.

Coulling, A.J., Goupee, A.J., Robertson, A.N., Jonkman, J.M., 2013. Importance of second-order difference-frequency wave-diffraction forces in the validation of a fast semi- submersible floating wind turbine model. In: ASME 32nd International Conference on Ocean, Offshore and Artic Engineering. https://doi.org/10.1115/OMAE2013-10308.

Coulling, A.J., Goupee, A.J., Robertson, A.N., Jonkman, J.M., Dagher, H.J., 2013. Validation of a FAST semi-submersible floating wind turbine numerical model with DeepCwind test data. J. Renew. Sustain. Energy 5. https://doi.org/10.1063/1.4796197.

DNV, 2007. DNV-RP-C205 Environmental Conditions and Environmental Loads.

Fontana, C.M., Arwade, S.R., DeGroot, D.J., Hallowell, S.T., Aubeny, C., Landon, M., Myers, A., Hajjar, J., Ozmultu, S., 2017. Multiline anchors for the OC4 semisubmersible floating system. In: International Society of Offshore and Polar Engineers, pp. 499–506.

Fontana, C.M., Hallowell, S.T., Arwade, S.R., DeGroot, D.J., Landon, M.E., Aubeny, C.P., Diaz, B., Myers, A.T., Ozmutlu, S., 2018. Multiline anchor force dynamics in floating offshore wind turbines. Wind Energy 1–14. https://doi.org/10.1002/we.2222.

Hall, M., 2017. MoorDyn User's Guide.

IEC 61400-3, 2009. Design Requirements for Offshore Wind Turbines.

Jonkman, J.M., Buhl Jr., M.L., 2005. FAST User's Guide. National Renewable Energy Laboratory. https://doi.org/10.2172/15020796.

Jonkman, B., Jonkman, J., 2016. FAST v8.16.00a-Bjj. National Renewable Energy Laboratory.

Jonkman, J.M., Butterfield, S., Musial, W., Scott, G., 2009. Definition of a 5-MW Reference Wind Turbine for Offshore System Development. National Renewable Energy Laboratory. https://doi.org/10.1002/ajmg.10175.

Jonkman, J.M., Robertson, A.N., Hayman, G.J., 2015. HydroDyn User's Guide and Theory Manual. National Renewable Energy Laboratory.

Latifah, A.L., Groesen, E. Van, 2012. Coherence and predictability of extreme events in irregular waves. Nonlinear Process Geophys. 19, 199–213. https://doi.org/10.5194/npg-19-199-2012.

London Array Operations and Maintenance Base, n.d. London Array Operations and Maintenance.

Mone, C., Hand, M., Bolinger, M., Rand, J., Heimiller, D., Ho, J., 2015. Cost of Wind Energy Review. National Renewable Energy Laboratory. https://doi.org/10.2172/1351062.

Nordee One Wind Farm Layout [WWW Document], 2017. URL. http://www.nordseeone.com/wind-farm/wind-farm-layout.html.

Offshore, 4C, 2018. Global Offshore Wind Farms Database [WWW Document]. URL. http://www.4coffshore.com/windfarms/. accessed 4.11.18.

Ormonde Development, 2005. Ormonde Project Environmental Impact Asssessment.

Peire, K., Nonneman, H., Bosschem, E., 2009. Gravity base foundations for the thornton bank offshore wind farm. Terra Aqua (Engl. Ed.) 19–29.

Robertson, A.N., Jonkman, J.M., Goupee, A.J., Coulling, A.J., Prowell, I., Browning, J., Masciola, M.D., Molta, P., 2013. Summary of conclusions and recommendations drawn from the deepcwind scaled floating offshore wind system test campaign. In: ASME 2013 32nd International Conference on Ocean, Offshore and Arctic Engineering. https://doi.org/10.1115/OMAE2013-10817.

Robertson, A., Jonkman, J., Masciola, M., Song, H., Goupee, A., Coulling, A., Luan, C., 2014. Definition of the Semisubmersible Floating System for Phase II of OC4. National Renewable Energy Laboratory. https://doi.org/10.2172/1155123.

Sarpkaya, T., Isaacson, M., 1981. Mechanics of Wave Forces on Offshore Structures. Van Nostrand Reinhold Co.

Sergeeva, A., Slunyaev, A., 2013. Rogue waves , rogue events and extreme wave kinematics in spatio-temporal fields of simulated sea states. Nat. Hazards Earth Syst. Sci. 13, 1759–1771. https://doi.org/10.5194/nhess-13-1759-2013.

Shemer, L., Sergeeva, A., 2009. An experimental study of spatial evolution of statistical parameters in a unidirectional narrow-banded random wavefield. Geophys. Res. 114. https://doi.org/10.1029/2008JC005077.

Spyroudi, A., 2016. Cost Modelling Analysis of Floating Wind Technologies: Assessing the Potential of TLPWIND.

Statoil, 2015. Hywind Scotland Pilot Park: Environmental Statement.

Statoil, 2016. The Development of Hywind Scotland Pilot Park [WWW Document]. URL. http://marine.gov.scot/datafiles/lot/hywind/Pre-application_consultation_report. accessed 1.1.17.

U.S. Department of Energy, 2016. Offshore Wind Technologies Market Report.

Viselli, A.M., Goupee, A.J., Dagher, H.J., Allen, C.K., 2016. Design and model confirmation of the intermediate scale VolturnUS floating wind turbine subjected to its extreme design conditions offshore Maine. Wind Energy 19, 1161–1177. https://doi.org/10.1002/we.1886.